

# In Situ Background Estimation in Quantitative Fluorescence Imaging

Tsai-Wen Chen,\* Bei-Jung Lin,\* Edgar Brunner,<sup>†</sup> and Detlev Schild\*

\*Institute of Physiology, and <sup>†</sup>Department of Medical Statistics, University of Göttingen, Göttingen, Germany

**ABSTRACT** Fluorescence imaging of bulk-stained tissue is a popular technique for monitoring the activities in a large population of cells. However, a precise quantification of such experiments is often compromised by an ambiguity of background estimation. Although, in single-cell-staining experiments, background can be measured from a neighboring nonstained region, such a region often does not exist in bulk-stained tissue. Here we describe a novel method that overcomes this problem. In contrast to previous methods, we determined the background of a given region of interest (ROI) using the information contained in the temporal dynamics of its individual pixels. Since no information outside the ROI is needed, the method can be used regardless of the staining profile in the surrounding tissue. Moreover, we extend the method to deal with background inhomogeneities within a single ROI, a problem not yet solved by any of the currently available tools. We performed computer simulations to demonstrate the accuracy of our method and give example applications in ratiometric calcium imaging of bulk-stained olfactory bulb slices. Converting the fluorescence signals into  $[Ca^{2+}]$  gives resting values consistent with earlier single-cell staining results, and odorant-induced  $[Ca^{2+}]$  transients can be quantitatively compared in different cells. Using these examples we show that inaccurate background subtraction introduces large errors (easily in the range of 100%) in the assessment of both resting  $[Ca^{2+}]$  and  $[Ca^{2+}]$  dynamics. The proposed method allows us to avoid such errors.

## INTRODUCTION

Fluorescence imaging of neuron populations is a powerful and widely used technique to study the brain's functional organization and dynamics (1–3). The technique not only enables researchers to probe a broad spectrum of physiological parameters (e.g., concentration of intracellular key ions, membrane potentials, etc.), but also gives information about both their spatial distribution and temporal dynamics. Using membrane-permeable fluorescent indicators (4,5) and optimized staining protocols (6,7) allow cells to be efficiently stained in a minimally invasive manner. This offers the possibility to monitor the activities in a large number of neurons in functionally preserved slices (2,8), and recently, in vivo (3,6,9). Fluorescence imaging of bulk-stained neurons has provided numerous important insights into the operation of network circuits. Recently, it has been used to demonstrate a repetitive multineuronal activation sequence (2), large-scale oscillatory activities in immature networks (8), and a detailed functional architecture in the visual cortex (3).

Despite these numerous advantages, imaging in bulk-stained tissue often suffers from an ambiguity of background estimation, which has been considered a major drawback of this powerful technique (5,10–12). Due to an excess of dye molecules introduced during the staining procedure and a tendency of membrane-permeable dyes to accumulate in intracellular compartments (13,14), background signals in bulk-stained tissue are both prominent and highly inhomogeneous compared to measurements performed in cultures,

in dissociated cells, or in experiments where cells are stained by microinjection, one at a time. In addition, accurate background estimation is often difficult or even impossible, because staining in neighboring cells and background inhomogeneities often preclude the use of a neighboring unstained region for background measurements.

Inaccurate background assessment seriously complicates a quantitative evaluation of fluorescence imaging experiments. Typically, to compare signals in different cells, normalized fluorescence intensities  $F/F_0$  or fluorescence ratios at different excitation wavelengths (15) are used to cancel the effects in dye concentration, optical pathlengths, excitation intensities, and detector efficiencies. However, both strategies can only yield meaningful results if the background of the detected signal is taken into account. In addition, since backgrounds affect the denominator in both measures, subtracting imprecise values will easily lead to large errors. Equally serious problems are encountered when converting fluorescence signals into the corresponding physiological parameters, e.g., intracellular  $[Ca^{2+}]$ . Well-known methods exist for  $[Ca^{2+}]$  quantification (15–17). However, using background-free fluorescence signals is a prerequisite for their successful application.

Here, we present a novel image-processing algorithm that estimates the background of a given region of interest (ROI) by exploiting the information contained in the intensity dynamics of its individual pixels. The major advantage of this approach is its ability to estimate the background unambiguously using only the fluorescence data within the respective ROI. Thus, the method does not require additional background measurements and can be used independently of the staining in neighboring tissue. Furthermore, we extended the method to deal with intra-ROI background inhomogeneities,

Submitted July 18, 2005, and accepted for publication December 5, 2005.

Address reprint requests to Detlev Schild, Dept. of Neurophysiology and Cellular Biophysics, Institute of Physiology, University of Göttingen, Humboldtallee 23, D37073, Göttingen, Germany. Tel.: 49-551-395915; Fax: 49-551-398399; E-mail: dschild@gwdg.de.

© 2006 by the Biophysical Society

0006-3495/06/04/2534/14 \$2.00

doi: 10.1529/biophysj.105.070854

which occur frequently in bulk-stained tissue but cannot be estimated with any of the currently available methods. We exemplify our method using ratiometric calcium imaging in bulk-stained olfactory bulb slices. On the one hand, our results were consistent with previous  $[Ca^{2+}]$  estimates using single-cell staining methods. On the other hand, they show that inaccurate background subtraction introduces marked and uncontrollable errors.

## THEORY

### The fluorescence signal of a region of interest

A region of interest is a subset of image pixels, the intensities of which are analyzed as a whole. Thus for a properly selected ROI, the fluorescence intensity of its individual pixels are assumed to follow a common physiological variable, e.g., the concentration of an intracellular ion species. Generally, the intensity time traces of ROI pixels are not identical but amplitude-scaled variants of a common waveform. The scaling factors reflect the optical pathlengths in wide field microscopy, or, in confocal microscopy, the fraction of the focal volume occupied by the imaged compartment. With  $u_i$  being the scaling factor of the  $i^{\text{th}}$  ROI pixel, and with  $f(t)$  being the physiological parameter-dependent waveform that is common to all pixels, the fluorescence signal of the  $i^{\text{th}}$  pixel can be written as

$$F_i(t) = u_i f(t) \quad (i = 1, 2, \dots, q). \quad (1)$$

Here,  $q$  is the number of pixels in the selected ROI.

### Homogeneous background within ROI

In real measurements, the signal is contaminated by noise and a constant background that is the sum of nonspecific staining, tissue autofluorescence, scattering, and detector offset. Let  $y_i(t)$  be the measured intensity time trace of the  $i^{\text{th}}$  ROI pixel,

$$y_i(t) = u_i f(t) + b + n_i(t), \quad (2)$$

with  $b$  and  $n_i(t)$  denoting background and noise, respectively. Our goal is to derive the common waveform  $f(t)$ , the scaling factors  $u_i$ , and the background  $b$  from the measured intensities  $y_i(t)$ . This can be done by first splitting Eq. 2 into a time-average and a time-varying part. With the overbar symbol denoting time-average, we have

$$\bar{y}_i = \bar{f} u_i + b + \bar{n}_i \quad (3)$$

and

$$\tilde{y}_i(t) = u_i \tilde{f}(t) + \tilde{n}_i(t), \quad (4)$$

where  $\tilde{y}_i(t) = y_i(t) - \bar{y}_i$ ,  $\tilde{f}(t) = f(t) - \bar{f}$ , and  $\tilde{n}_i(t) = n_i(t) - \bar{n}_i$ .

This formulation decomposes the estimation of  $u_i$ ,  $\tilde{f}(t)$ , and the estimation of  $b$  into two separate problems. Based on

Eq. 4, we first derived an estimator of  $u_i$  and  $\tilde{f}(t)$  using the maximum-likelihood (ML) method (18) (see next section). After an estimate of  $u_i$  is available, we then exploit the linear relationship between  $\bar{y}_i$  and  $u_i$  (Eq. 3). The background  $b$  as well as  $\bar{f}$  can be determined as the intercept and the slope of the regression line through the  $(\bar{y}_i, u_i^*)$  pairs.

The pure fluorescence signal can be computed from  $u_i^*$ ,  $\tilde{f}^*(t)$ , and  $\bar{f}$  as

$$F_i^*(t) = u_i^* (\tilde{f}^*(t) + \bar{f}). \quad (5)$$

With this procedure, the background-free signal of a given ROI can be extracted without using any other information except the data of that ROI itself.

### Maximum likelihood estimation of $u_i$ and $\tilde{f}(t)$

Our method exploits the linear relationship between  $\bar{y}_i$  and  $u_i$  (Eq. 3) to estimate background. An accurate estimation of  $u_i$  is therefore essential for the proper functioning of the algorithm. The easiest way to estimate the scaling factors  $u_i$  is by calculating the standard deviation of the intensity traces,  $\tilde{y}_i(t)$ . Unfortunately, the standard deviation of  $\tilde{y}_i(t)$  invariably overestimates the true  $u_i$ -value.

To overcome this problem, we derived an improved estimator of  $u_i$  and  $\tilde{f}(t)$  using the ML method (18). The ML method models the experimental data as outcomes drawn from a probability distribution that depends on unknown parameters, in our case,  $u_i$  and  $\tilde{f}(t_j)$ , with  $t_j$  being discrete timepoints. The parameters of the distribution were estimated such that they make the observed data most likely under the assumed probability model. The estimator thus obtained is asymptotically unbiased and shows the smallest error variance in the large sample limit (18). These superior statistical properties have rendered the ML estimation a method of choice in applications that require accurate and reliable parameter estimation (19–22).

To simplify our derivation, we first assume the following compact notations. Suppose the image sequence contains  $p$  images taken at times  $t_1, t_2, \dots, t_p$ , we represent the fluorescence intensity traces pixelwise as  $p$ -dimensional vectors,  $\mathbf{y}_i = [y_i(t_1), y_i(t_2), \dots, y_i(t_p)]'$ , with the prime symbol denoting vector transpose. Similarly, we defined  $\mathbf{f} = [f(t_1), f(t_2), \dots, f(t_p)]'$ ,  $\mathbf{b} = b \mathbf{1}_p$ , and  $\mathbf{n}_i = [n_i(t_1), n_i(t_2), \dots, n_i(t_p)]'$ . Here,  $\mathbf{1}_p = [1, 1, \dots, 1]'$  denotes the  $p$ -dimensional vector of ones. Then Eq. 2 becomes

$$\mathbf{y}_i = u_i \mathbf{f} + \mathbf{b} + \mathbf{n}_i. \quad (6)$$

In most imaging applications, the number of photons per exposure interval is sufficiently large to approximate the photon shot-noise by a Gaussian distribution. Here we assume the elements of  $\mathbf{n}_i$  as independent Gaussian random variables with zero mean and variance  $\sigma_n^2$ .

Define  $\mathbf{w}_0 = (1/p)\mathbf{1}_p$ . The separation of Eq. 2 into a time average (Eq. 3) and a time varying (Eq. 4) part is equivalent to

an orthogonal decomposition of the vector space  $R^p$  into two subspaces:  $W_0 = \text{span}\{\mathbf{w}_0\}$ , and its orthogonal complement  $W^\perp$ . Projecting both sides of Eq. 6 onto  $W_0$  gives the time-averaged part, while their projections onto  $W^\perp$  yields the time-varying part:

$$\tilde{\mathbf{y}}_i = u_i \tilde{\mathbf{f}} + \tilde{\mathbf{n}}_i. \quad (7)$$

Let  $\{\mathbf{w}_1, \mathbf{w}_2, \dots, \mathbf{w}_{p-1}\}$  be an orthonormal basis of the  $(p-1)$ -dimensional space  $W^\perp$ ; writing the components of Eq. 7 with respect to this basis yields

$$\tilde{\zeta}_{ik} = u_i \tilde{\xi}_k + \tilde{\varepsilon}_{ik} \quad (k = 1, 2, \dots, p-1), \quad (8)$$

where  $\tilde{\zeta}_{ik} = \mathbf{w}'_k \tilde{\mathbf{y}}_i$ ,  $\tilde{\xi}_k = \mathbf{w}'_k \tilde{\mathbf{f}}$  and  $\tilde{\varepsilon}_{ik} = \mathbf{w}'_k \tilde{\mathbf{n}}_i$ .

Since the  $\tilde{\varepsilon}_{ik}$  are linear combinations of Gaussian RVs, the  $\tilde{\varepsilon}_{ik}$  are Gaussian, too. In addition, the expectations,  $E\{\tilde{\varepsilon}_{ik}\} = 0$ , and the covariances  $E\{\tilde{\varepsilon}_{ik}\tilde{\varepsilon}_{lm}\} = \mathbf{w}'_k E\{\tilde{\mathbf{n}}_i \tilde{\mathbf{n}}'_l\} \mathbf{w}_m = \sigma_n^2 \delta_{il} \delta_{km}$ . Thus,  $\tilde{\varepsilon}_{ik}$  are independent Gaussian RVs with zero mean and variance  $\sigma_n^2$ . The probability distribution of  $\tilde{\zeta}_{ik}$ , given the constant parameters  $u_i$  and  $\tilde{\xi}_k$ , can thus be written as

$$p(\tilde{\zeta}_{ik} | u_i, \tilde{\xi}_k) = \frac{1}{(2\pi\sigma_n^2)^{\frac{(p-1)}{2}}} \exp\left\{-\frac{1}{2\sigma_n^2} \left(\sum_{i,k} (\tilde{\zeta}_{ik} - u_i \tilde{\xi}_k)^2\right)\right\}. \quad (9)$$

Once the observations  $\tilde{\zeta}_{ik}$  are given, the probability-density function is a function of  $u_i$  and  $\tilde{\xi}_k$  alone, and the value of  $u_i$  and  $\tilde{\xi}_k$  that maximize the above probability-density function is their most likely value,

$$\begin{aligned} (u_i^*, \tilde{\xi}_k^*) &= \arg \max_{u_i, \tilde{\xi}_k} p(\tilde{\zeta}_{ik} | u_i, \tilde{\xi}_k) \\ &= \arg \min_{u_i, \tilde{\xi}_k} \left( \sum_{i,k} (\tilde{\zeta}_{ik} - u_i \tilde{\xi}_k)^2 \right). \end{aligned} \quad (10)$$

Note that multiplying all  $u_i$  and dividing all  $\tilde{\xi}_k$  by the same nonzero constant leads to the same density function. To remove this ambiguity and make the optimization solution unique, we impose the additional constraint  $\sum_k \tilde{\xi}_k^2 = 1$ . The optimization problem is equivalent to finding  $u_i$  and  $\tilde{\mathbf{f}} \in W^\perp$ , such that

$$S = \sum_{i=1}^q |\tilde{\mathbf{y}}_i - u_i \tilde{\mathbf{f}}|^2 \quad (11)$$

is minimized under the constraint  $|\tilde{\mathbf{f}}|^2 = 1$ .

This optimization problem can be solved analytically (see Appendix A) by choosing

$$\tilde{\mathbf{f}}_{\text{ML}}^* = \beta_1, \quad (12)$$

$$u_{i,\text{ML}}^* = \tilde{\mathbf{y}}_i' \tilde{\mathbf{f}}_{\text{ML}}^*, \quad (13)$$

where  $\beta_1$  is the unit-length eigenvector of the matrix  $R = (\sum_{i=1}^q \tilde{\mathbf{y}}_i \tilde{\mathbf{y}}_i')$  associated to its maximum eigenvalue.

In other words, the common waveform  $\tilde{\mathbf{f}}$  is first estimated by performing eigenanalysis of the matrix  $R$  formed by the observed data. The scaling factors  $u_{i,\text{ML}}^*$  are then obtained as

the inner product between the observed intensity trace  $\tilde{\mathbf{y}}_i$  and the estimated common waveform  $\tilde{\mathbf{f}}_{\text{ML}}^*$ .

In summary, our method consists of the following steps:

1. Calculate the time-averaged fluorescence intensity  $\bar{y}_i$  for each pixel and then obtain  $\tilde{y}_i(t) = y_i(t) - \bar{y}_i$ .
2. Estimate  $\tilde{\mathbf{f}}_{\text{ML}}^*$  as the unit-length eigenvector of the matrix  $R = (\sum_{i=1}^q \tilde{\mathbf{y}}_i \tilde{\mathbf{y}}_i')$  associated to its largest eigenvalue. The scaling factors  $u_i$  can be estimated as  $u_{i,\text{ML}}^* = \tilde{\mathbf{y}}_i' \tilde{\mathbf{f}}_{\text{ML}}^*$ .
3. Fit a line to the  $(\bar{y}_i, u_i^*)$  pairs and then estimate  $f$  as the slope and  $b$  as the intercept of the fitted line.
4. The background-free fluorescence can be calculated as  $F_i^*(t) = u_i^*(\tilde{f}^*(t) + f)$ .

In Results, below, we delineate the steps of this procedure using calcium-imaging data taken from olfactory bulb slices of *Xenopus laevis* tadpoles.

### Inhomogeneous background within a single ROI

In bulk-stained tissue, the background can frequently be inhomogeneous even within a single ROI. This occurs, for example, when the selected ROI contains contaminations from clustering of intra- or extracellular dye molecules or other fluorescent structures. Let  $p_i \geq 0$  be the additional background contamination at the  $i^{\text{th}}$  pixel. Equation 3 then becomes

$$\bar{y}_i = \bar{f} u_i + b + \bar{n}_i + p_i. \quad (14)$$

For pixels with no additional background,  $p_i = 0$ . Accordingly, they form a line with slope  $\bar{f}$  and intercept  $b$  in the  $\bar{y}_i(u_i)$  plot. In contrast, contaminated pixels show  $p_i > 0$ , thus tend to reside above this line. Therefore, the vertical distance between the pixels and the regression line,  $d_i = \bar{y}_i - \bar{f} u_i^* - b$ , is a measure of additional background.

To distinguish whether the observed  $d_i$  is due to random error of  $\bar{y}_i$  and  $u_i^*$ , or whether a significant additional background occurred, we estimated the variation of  $d_i$  under homogeneous background assumption. We first estimate  $\sigma_n^2$  by calculating the variance of  $(\bar{y} - u_i^* \bar{f})$ , the part of the measured signal that is not explained by the model. We then showed that  $d_i$  has a distribution with zero mean and its variance can be related to  $\sigma_n^2$  by  $\sigma_d^2 = (\bar{f}^2 + (1/p))\sigma_n^2$  (see Appendix B). In the absence of background inhomogeneity,  $d_i$  is expected to distribute within a  $\pm 3 \sigma_d$  range. A  $d_i$ -value much larger than this variation is unlikely to occur by chance, and suggests the presence of an additional background.

We identify the pixels containing additional background using the following iterative procedure. First, assuming  $p_i = 0 \forall i$ , we obtained a first estimate of  $\bar{f}$  and  $b$  by linear regression of all  $(\bar{y}_i, u_i^*)$  pairs. We then calculated the  $d_i$  of each of the pixels and checked whether they are all smaller than  $4\sigma_d$ . If not, we exclude the pixel with maximum  $d_i$ -value assuming the presence of additional background. A new estimate for  $\bar{f}$  and  $b$  was then obtained by fitting the remaining pixels. The procedure was repeated until all remaining pixels fell within a  $4\sigma_d$ -range around the regression line. These pixels now

constitute a region where the additional background  $p_i$  is indistinguishable from zero. Thus, their common background value can be estimated as the intercept of the regression line  $b$ . On the other hand, the excluded pixels have a significant nonzero  $p_i$ , and  $(d_i + b)$  was taken as the background of those pixels.

## MATERIALS AND METHODS

### Slice preparation

Tadpoles of *Xenopus laevis* (stage 53–55) (23) were chilled in a mixture of ice and water, and decapitated as approved by the Göttingen University Committee for Ethics in Animal Experimentation. A block of tissue containing olfactory mucosae, intact olfactory nerves, and most of the brain was cut out and kept in physiological saline (98 mM NaCl, 2 mM KCl, 1 mM CaCl<sub>2</sub>, 2 mM MgCl<sub>2</sub>, 5 mM glucose, 5 mM Na-pyruvate, 10 mM HEPES; 230 mOsm, pH 7.8; all chemicals were from Sigma, Deisenhofen, Germany). The tissue was glued onto the stage of a vibroslicer (VT 1000S, Leica, Bensheim, Germany) and the dorsal part of the olfactory bulb was sliced off. The olfactory mucosae and nerves were kept intact. The nose-olfactory bulb preparation was transferred to a recording chamber, and 200  $\mu$ L of bath solution containing 50  $\mu$ M of FURA-2/AM or Fluo-4/AM (Molecular Probes, Eugene, OR) was added. The slice was incubated for 30 min at room temperature and then rinsed with bath solution for at least 30 min under a bath flow at a rate of 550  $\mu$ L min<sup>-1</sup> in the recording setup. A detailed description of the preparation is given in Czesnik et al. (24).

### Calcium imaging

Ratiometric calcium measurements with FURA-2 were performed using an upright microscope (Axioskop 2, Zeiss, Göttingen, Germany) with a 40 $\times$  (NA = 0.9) objective. Alternating excitation wavelengths at 350 and 380 nm were provided by a custom-built monochromator consisting of a Xenon lamp, a galvanometer-driven mirror, appropriate filters, and a shutter. Pairs of fluorescence images of the olfactory bulb were taken at 4–5 Hz using a frame transfer, back-illuminated CCD camera (Micromax, VisiTron, Munich, Germany). Galvanometer, shutter as well as the CCD's acquisition and recording software were synchronized by a custom-built microcontroller programmed in C language (25).

FURA-2 calibration was performed in unstained slices.  $R_{\min}$  and  $R_{\max}$  (fluorescence ratios at zero [Ca<sup>2+</sup>]<sub>i</sub> and at [Ca<sup>2+</sup>]<sub>i</sub> levels saturating FURA-2, respectively) were determined by loading OB neurons through a patch pipette with intracellular solution containing 10 mM EGTA and 10 mM CaCl<sub>2</sub>, respectively. The effective binding constant ( $K_{\text{eff}}$ ) was determined using intracellular solution containing 5 mM CaCl<sub>2</sub> and 10 mM BAPTA. Under our experimental conditions  $R_{\min}$ ,  $R_{\max}$ , and  $K_{\text{eff}}$  were determined to be 0.46, 6.12, and 1680 nM, respectively. The pipette resistance was in the range of 3–4 M $\Omega$ .

Calcium imaging with Fluo-4/AM was performed using a confocal laser scanning microscope (Zeiss LSM 510/Axiocvert 100 M) with a 40 $\times$  (NA = 1.3) oil immersion objective. Fluorescence images (excited at 488 nm) of the olfactory bulb were acquired at 2 Hz. The pinhole was set to 200  $\mu$ m, resulting in <2.5- $\mu$ m optical slices. Photomultiplier voltage was sampled at 12 bits. Amplifier gain and detector offset were adjusted such that neither saturation nor threshold cutoff occurred.

Image analysis was performed using custom programs written in MatLab (The MathWorks, Natick, MA). Acquired image sequences were analyzed directly without any spatial or temporal prefiltering. The algorithms are described in Theory, above.

### Computer simulation

#### Data model

We generated fluorescence images of a round object with time-varying intensities to mimic the experimental ROI data. The scaling factor of the  $i^{\text{th}}$

pixel within the object was set to  $u_i = \sqrt{R^2 - x_i^2 - y_i^2}$ , with  $R$  being the radius of the object and  $x_i$ ,  $y_i$  being the spatial location of the pixel. The fluorescence time course  $f(t)$  was taken as the sum of individual events each being characterized by a sudden rise followed by an exponential decay to mimic the intracellular [Ca<sup>2+</sup>]<sub>i</sub> waveform. The onset timing of each event was determined according to a Poisson point process. The generated  $f(t)$  were first normalized such that  $\sum_k |f(t_k) - \bar{f}|^2 = 1$  and then multiplied by  $u_i$  to yield the ROI's signal fluorescence trace  $y_i(t) = u_i f(t)$ . To each pixel, we added a known background value and random noise with variance specified by the given SNR. The data simulated this way were then analyzed by background estimation algorithms, and the results were compared to the true background. In our simulations, we treated the background level  $b$  and the noise variance  $\sigma_n^2$  as two independent parameters, and their effects were studied separately.

We evaluate the algorithm's performance as a function of the following four parameters: 1),  $\overline{SNR}$ ; 2), number of timepoints ( $p$ ); 3), number of ROI pixels ( $q$ ); and 4), the coefficient of variation ( $CV_u$ ) of the  $u_i$ . Here,

$$SNR_i \triangleq \sqrt{\frac{\sum_k (u_i \tilde{f}_k)^2}{p}} / \sigma_n \quad (15)$$

is the signal/noise ratio of the  $i^{\text{th}}$  pixel, and

$$\overline{SNR} \triangleq \frac{1}{q} \sum_{i=1}^q SNR_i \quad (16)$$

is the  $SNR_i$  value averaged over a given region of interest. The coefficient of variation of  $u_i$  is defined by

$$CV_u \triangleq \frac{SD(u_i)}{\text{Mean}(u_i)}. \quad (17)$$

This parameter measures the spread of the  $u_i$ -values and is normalized by their mean value. It thus depends only on the geometry of the imaged object but not the absolute magnitude of the  $u_i$ -values. We expect the performance of the algorithm depends on  $CV_u$  because the algorithm requires a certain spread of the  $u_i$  to ensure meaningful linear regression, i.e., the algorithm cannot work for  $CV_u = 0$ . In simulation experiments designed to study the effect of  $CV_u$ , the  $u_i$ -values were generated as  $u_i = (R^2 - x_i^2 - y_i^2)^\alpha$ . Varying  $\alpha$  from 0.125 to 1 changes the  $CV_u$  monotonically from 0.14 to 0.62, thus allowing us to systematically vary the  $CV_u$  value while keeping the number of pixels ( $q$ ) constant.

### Estimation algorithms

Three different algorithms (abbreviated as SD, ML<sub>1</sub>, ML<sub>2</sub>) were implemented and their performance was compared. While the SD algorithm uses the standard deviation of  $y_i(t)$  to estimate  $u_i$ , the ML algorithms estimate  $u_i$  using the proposed maximum-likelihood method. The difference between the ML<sub>1</sub> and the ML<sub>2</sub> algorithm is the way they fit the  $(\bar{y}_i, u_i^*)$  pairs. The ML<sub>1</sub> algorithm obtains  $b$  and  $\bar{f}$  by fitting  $\bar{y}_i$  against  $u_i$ , i.e., the parameters  $b$  and  $\bar{f}$  were estimated to minimize the sum of squared vertical distances of the  $(\bar{y}_i, u_i^*)$  pairs with respect to the regression line,

$$\sum_i (\Delta \bar{y}_i)^2 = \sum_i |\bar{y}_i - (u_i^* \bar{f} + b)|^2. \quad (18)$$

On the other hand, the ML<sub>2</sub> algorithm finds  $b$  and  $\bar{f}$  by minimizing the sum of squared horizontal distances,

$$\sum_i (\Delta u_i^*)^2 = \sum_i \left| u_i^* - \frac{\bar{y}_i - b}{\bar{f}} \right|^2. \quad (19)$$

### Estimation error

An algorithm is said to be precise if the value it estimates falls within a narrow range. However, a measurement can be precise without being

accurate; that is, the results may be systematically biased toward an incorrect value. To assess both types of error, we run each algorithm 1000 times for a given condition and used the standard deviation ( $\sigma$ ) of the estimated values as a measure for the algorithm's precision. The accuracy was measured by the statistical bias, which is defined as the difference between the average of the estimated values and the known true value.

## RESULTS

### Homogeneous background

We performed calcium-imaging experiments in brain slices of *Xenopus laevis* tadpoles that contained the olfactory mucosae, intact olfactory nerves, and most of the brain (24,26). Loading the slices with FURA-2/AM stained large populations of olfactory bulb neurons (Fig. 1 A). This allowed us to study both ongoing and odorant-modulated activities in a large number of cells at subcellular resolution (Fig. 1 B). However, in contrast to neurons individually stained through a patch pipette (Fig. 1 C), finding an unambiguous region for background estimation was virtually impossible in bulk-stained tissue.

Fig. 2 A shows a cell that exhibited spontaneous  $[Ca^{2+}]$  fluctuations during the recording period. From the temporal information of each pixels' fluorescence data (Fig. 2 B), we estimated the most likely underlying  $[Ca^{2+}]$ -dependent dynamic waveform,  $\hat{f}(t)$  (Fig. 2 C, top), and the scaling factors of each pixel  $u_i$  using the ML method described in Theory, above. The estimated  $u_i$  are shown as a color-coded map (Fig. 2 C, bottom). Extrapolating the regression line of the  $(\bar{y}_i, u_i)$  pairs to the value  $u_i = 0$  gives the ROI intensity where the signal contribution vanishes (Fig. 2 D, arrow). This intensity therefore represents the background of this ROI.

### Background inhomogeneity within a single ROI

Subtracting the same background value from each ROI pixel is justified if the background within the ROI is homogeneous. However, this is not necessarily the case in the complex environment of bulk-stained tissue where cells can easily receive additional background contamination from intra- or extracellular dye accumulation or other fluorescent structures. In the example shown in Fig. 3 A, a cell showing  $[Ca^{2+}]$  fluctuations is overlapped by two neighboring cells that stayed silent during the imaging period. Thus, choosing a ROI around the cell will result in an inhomogeneous background if any of those overlapping pixels were included. Additional background of a pixel results in its deviation from the regression line (Fig. 3 D). Thus, simple linear fitting to the  $(\bar{y}_i, u_i)$  pairs would yield an erroneous result.

This difficulty can be resolved by noting that the additional background affects the average intensities  $\bar{y}_i$  (Fig. 3 A) but not the scaling factors  $u_i$  (Fig. 3 B). Comparing two pixels with similar  $u_i$  (Fig. 3 C, the two marked pixels in Fig. 3, A, B, and D), the one having the larger  $\bar{y}_i$  must contain an additional background component. Thus, the vertical distances,  $d_i$ , of the pixels to the regression line are a measure of

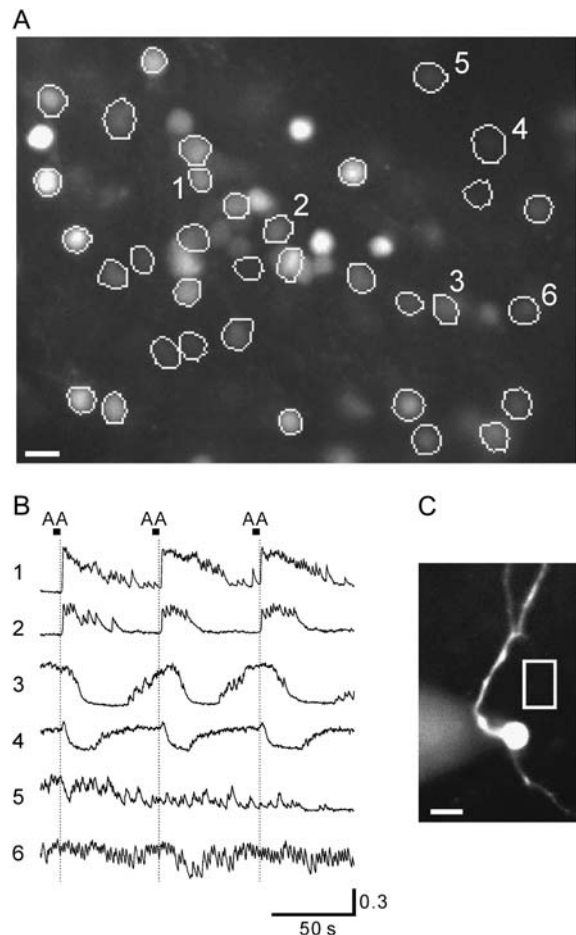


FIGURE 1 Fluorescence recordings from olfactory bulb slices of *Xenopus laevis* tadpoles bulk loaded with FURA-2/AM. (A) Image taken at 380-nm excitation. The fluorescence time courses of the indicated neurons are shown in B. Scale bar, 20  $\mu\text{m}$ . (B)  $[Ca^{2+}]$  dynamics of the neurons indicated in A. Odorant stimulations with a mixture of amino acids to the ipsilateral olfactory mucosa are indicated by the bars above the trace and the vertical lines. Fluorescence ratios,  $F_{350}/F_{380}$ , are shown without background subtraction. Background ambiguity in this type of experiments can be clearly seen in A. (C) FURA-2 image of a single olfactory bulb neuron stained through a patch pipette (out of focus). In this type of experiments, background can be reliably measured from a nonstained region. Scale bar, 20  $\mu\text{m}$ .

additional background, in this case the fluorescence from neighboring cells. We adopted an iterative test-and-exclude procedure (see Theory, above) to identify pixels with  $d_i$ -values too large to be explained by random noise (red pixels in Fig. 3 D). Displaying  $d_i$ , i.e., the additional background, as a spatial map clearly revealed the structure of the contaminating sources (Fig. 3 D, inset).

Analyzing the fluorescence signals this way allows us to decompose the original data (Fig. 4 A) into the signals of interest (Fig. 4 B) and contaminating patterns that include background and noise (Fig. 4 C). The signals are amplitude-scaled versions of a common function, while the background and the noise are the time-average and the time-varying part of the data that does not show such scaling.

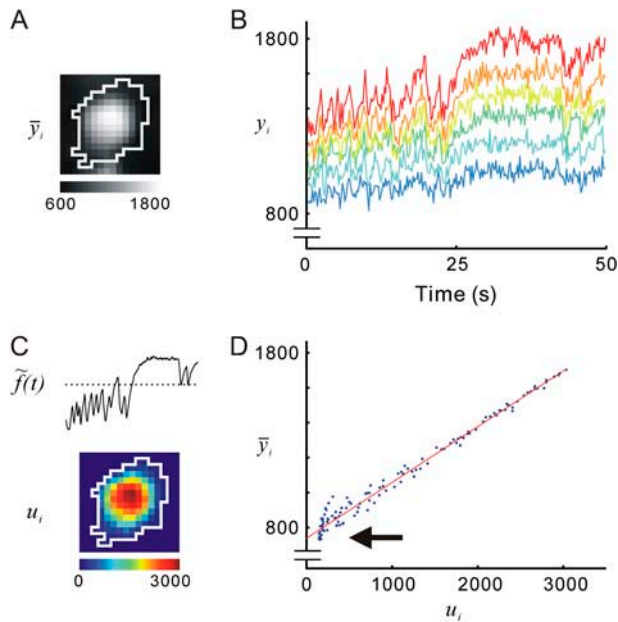


FIGURE 2 Estimating the background of a ROI using its own fluorescence data. (A) FURA-2 image of a cell exhibiting spontaneous  $[Ca^{2+}]$  activities (380 nm excitation). (B)  $[Ca^{2+}]$ -dependent fluorescence traces of six example pixels within this ROI. (C) The common concentration-dependent waveform  $\tilde{f}(t)$  (top) and the scaling factors  $u_i$  (bottom, shown as a color-coded map) were estimated using the maximum likelihood method. Note the  $u_i$ -values approach zero at the cell boundary, whereas the average intensities (A) do not. (D) A regression line of the  $(\bar{y}_i, u_i)$  pairs is extrapolated to  $u_i = 0$ , which gives the background of this ROI (arrow, 741 a.u.).

### Computer simulation

To assess the performance of our algorithm, we carried out a series of modeling-based simulations to characterize the effects of several experimental parameters on the algorithm accuracy and precision. We first noted that the background error  $\Delta b$  did not depend on the absolute background value, but was proportional to the averaged true fluorescence of the ROI. This means that, with other parameters fixed, the background error was a constant fraction of the true ROI fluorescence, irrespective of the absolute background value. In the following, we thus represent the background error as  $\Delta b/\bar{F}$  rather than  $\Delta b/b$ .

### Comparison of different algorithms

The SD and the ML algorithms differ in the ways they estimate the scaling factors  $u_i$ . Although the standard deviation is a common measure of the amplitude of a time-varying signal, it always overestimates the true  $u_i$ , especially for pixels with small  $u_i$ -values (Fig. 5 A). The overestimation is prominent already at a relatively high signal/noise ratio, and leads to a severe underestimation of the true background (Fig. 5 A). In contrast, the ML estimator  $u_{i,ML}^*$  (Eq. 13) estimates the  $u_i$  much more accurately.

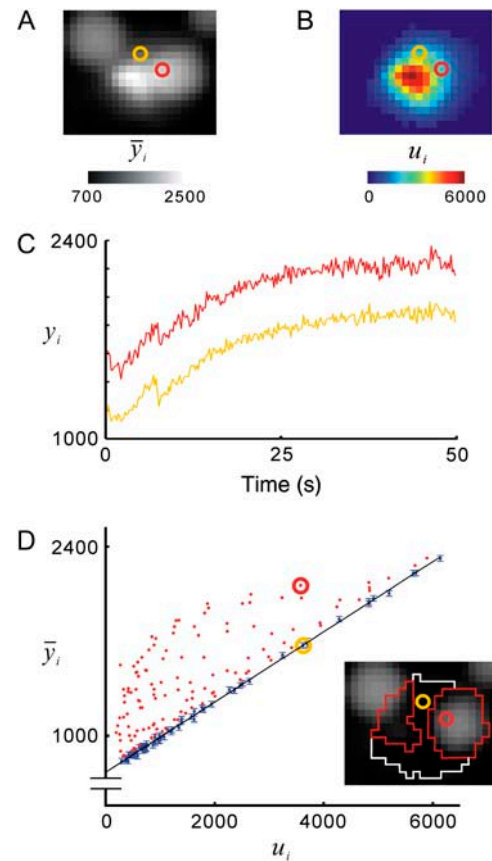


FIGURE 3 Estimation of intra-ROI background inhomogeneities. (A) A cell showing  $[Ca^{2+}]$ -dependent fluorescence fluctuation (middle) partly overlaps with two neighboring cells that stayed silent during the recording period. (B) The map of  $u_i$  reveal the contribution from the cell of interest. (C) Fluorescence traces of the two pixels marked in A, B, and D. Both pixels showed a similar scaling factor but the red pixel showed an additional constant offset, suggesting an additional background contamination. (D)  $(\bar{y}_i, u_i)$  pairs plotted as in Fig. 2 D using the data of this example. The ROI was partitioned into an homogeneous (blue dots) and an inhomogeneous (red dots) background region by the procedure described in Theory (see article). Linear regression through the blue pixels gives both  $\tilde{f}$  and a common background  $b$ . Displaying the vertical distances of the pixels to the regression line ( $d_i$ ) as a spatial map (inset) reveals the additional inhomogeneous background pattern.

At lower pixel signal/noise ratios, different linear fitting methods can give considerably different regression lines. This is illustrated in Fig. 5 B: the regression lines obtained by minimizing the squared vertical error (ML<sub>1</sub> method) or by minimizing the squared horizontal error (ML<sub>2</sub> method) can differ substantially, and the ML<sub>1</sub> method tends to give a higher background value than the ML<sub>2</sub> method.

### Bias as a function of $\overline{SNR}$ , $p$ , $q$ , and $CV_u$

We systematically varied four different parameters ( $\overline{SNR}$ ,  $p$ ,  $q$ , and  $CV_u$ ) and characterized their effects on the accuracy and precision of the three algorithms. As expected, the SD algorithm gives a background that is significantly biased

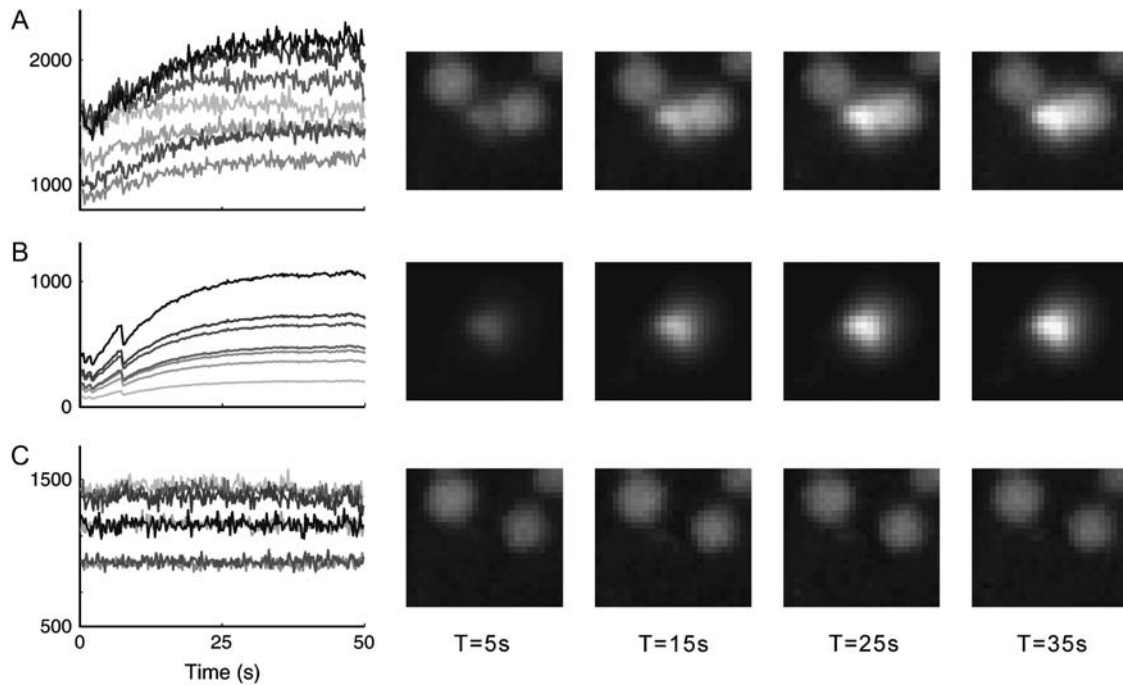


FIGURE 4 Decomposition of the measured data into signals of interest and contaminating patterns. (A) Original data. Example traces of seven selected pixels of the responsive cell are shown (*left*). A sequence of four fluorescence images acquired at the timepoints indicated below the images are shown (*right*). (B) Extracted signal fluorescence and (C) contamination including background and noise.

toward more negative values (Fig. 6 A, *left*). This negative bias was as large as  $-10\%$  even for the highest tested SNR ( $\overline{SNR} = 5$ ), and continued to grow for decreasing  $\overline{SNR}$ . The bias of the  $ML_1$  and the  $ML_2$  algorithm was indistinguishable from zero in the high SNR range. However, for the  $ML_1$  algorithm, a positive bias emerged for  $\overline{SNR} < 1$ , whereas the  $ML_2$  algorithm was unbiased even when the  $\overline{SNR}$  was as low as 0.2.

We also examined the effect of the number of timepoints ( $p$ ). At a fixed SNR ( $\overline{SNR} = 2$ ), the SD algorithm gave a bias

value more negative than  $-30\%$  for all  $p$  from 30 to 1000. The  $ML_1$  algorithm showed a slight positive bias when  $p < 500$ , while the bias of the  $ML_2$  algorithm was negligible for all  $p$ -values tested (Fig. 6 B, *left*). Similar results were obtained for the bias as a function of  $q$  and  $CV_u$  (data not shown). In summary, the SD algorithm significantly underestimates the true background under all conditions tested, and the  $ML_1$  algorithm shows a slight overestimation at smaller  $\overline{SNR}$ ,  $p$ , or  $CV_u$ . Remarkably, the  $ML_2$  algorithm

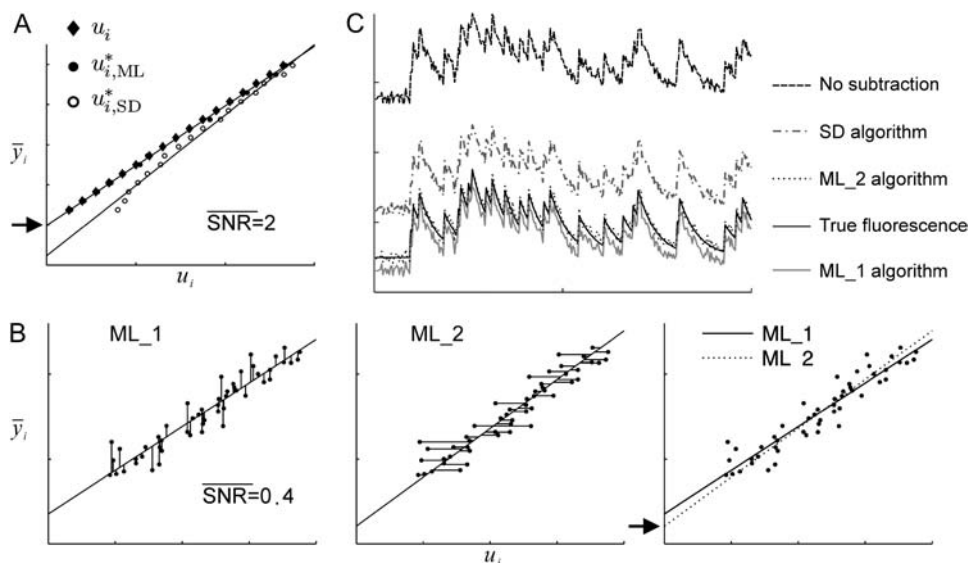


FIGURE 5 Comparison of three algorithms using computer simulation. (A) The standard deviation ( $u_{i,SD}^*$ ) overestimates the true  $u_i$ , which is especially significant for smaller  $u_i$ -values. This leads to a considerable underestimation of the background value (arrow, true background). (B) Minimizing the sum of vertical error (*left*,  $ML_1$  algorithm) or the sum of horizontal error (*middle*,  $ML_2$  algorithm) give different regression lines for the same data points (arrows, true background). (C) Simulated fluorescence trace after subtracting the background estimated by the algorithms indicated.

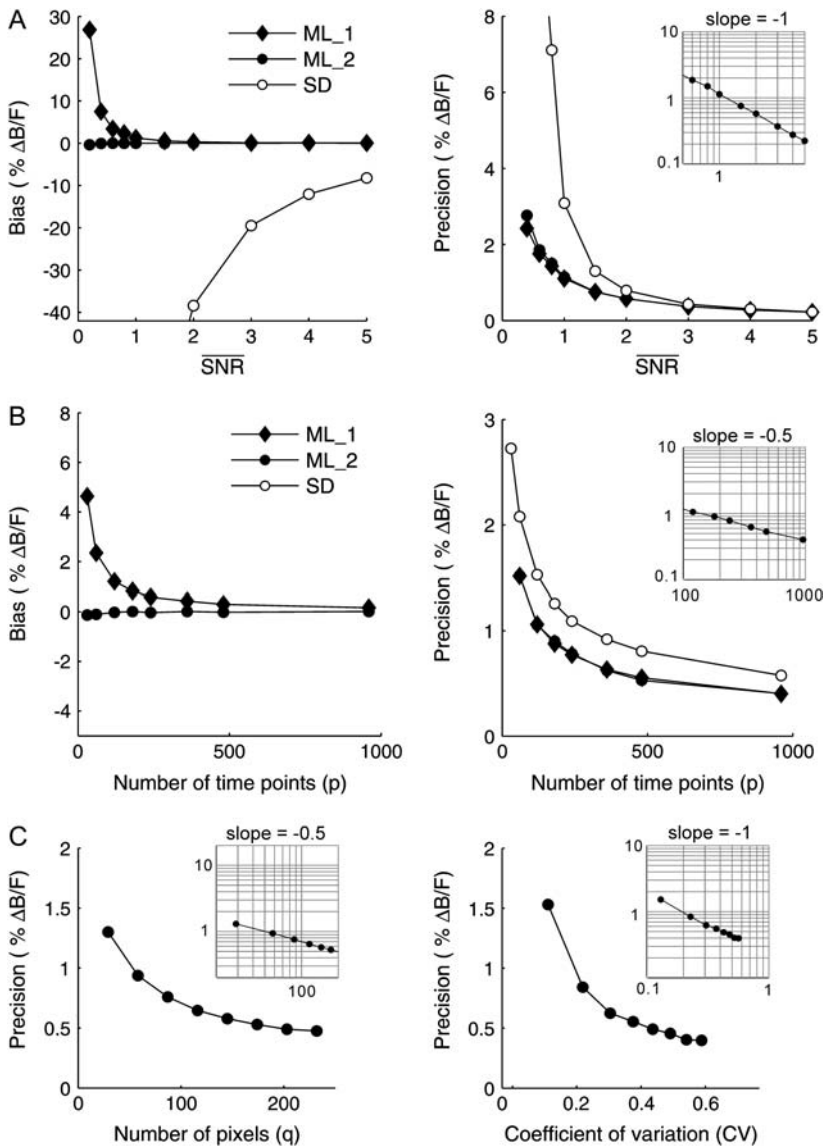


FIGURE 6 Bias and precision as a function of  $\overline{SNR}$ ,  $p$ ,  $q$ , and  $CV_u$  (A) Bias (left) and precision (right) as a function of  $\overline{SNR}$  ( $p = 480, q = 121, CV_u = 0.41$ ). (B) Bias (left) and precision (right) as a function of timepoints  $\overline{SNR} = 2, q = 121, CV_u = 0.41$ . The bias of the SD algorithm is more negative than -30% for all points tested, and therefore not shown in this graph. (C) Precision of the ML<sub>2</sub> algorithm as a function of pixel number  $q$  ( $\overline{SNR} = 2, p = 480, CV_u = 0.35$ ) and  $CV_u$  ( $\overline{SNR} = 2, p = 480, q = 121$ ). The background errors shown were all normalized by the mean true ROI fluorescence ( $\Delta b/\bar{F}$ ).

remains unbiased even for  $\overline{SNR}$  as low as 0.2 or the number of timepoints as few as 30.

### Precision as a function of $\overline{SNR}$ , $p$ , $q$ , and $CV_u$

We then characterized the algorithm precision, defined as the standard deviation ( $\sigma$ ) of the estimated outcomes, as a function of  $\overline{SNR}$ ,  $p$ ,  $q$ , and  $CV_u$ . Since the ML<sub>2</sub> algorithm is unbiased, we focused on the precision of the ML<sub>2</sub> algorithm.

The precision increases ( $\sigma$  decreases) monotonically as the SNR increases (Fig. 6 A, right). Even at the lowest tested SNR ( $\overline{SNR}$ ), the ML<sub>2</sub> algorithm gives precise background estimates ( $\sigma < 4\%$ ). That is, the ML<sub>2</sub> algorithm is expected to give a background error smaller than 4% in 66.7% of the trials, even at an  $\overline{SNR}$  as low as 0.2. Plotting  $\sigma$  against  $\overline{SNR}$  on a logarithmic scale (Fig. 6 A, right, inset) gives a straight

line with slope -1. Thus we conclude that  $\sigma$  is inversely proportional to  $\overline{SNR}$ .

The precision of the ML<sub>2</sub> algorithm also increases as  $p$ ,  $q$ , or  $CV_u$  increases (Fig. 6 B, right and 6 C). That is, the algorithm is more precise when the number of timepoints or the number of pixel is large, or when the  $u_i$  of the ROI pixels show a large variation. Plotting  $\sigma$  against  $p$  (Fig. 6 B, right, inset),  $q$  (Fig. 6 C, left, inset), and  $CV_u$  (Fig. 6 C, right, inset) gives straight lines with slopes of -0.5, -0.5, and -1, respectively. Thus, combined with the  $1/\overline{SNR}$  relationship, we give a formula to summarize the dependency of  $\sigma$  on the four parameters

$$\sigma = \frac{1}{\sqrt{p q \overline{SNR} CV_u}} \quad (20)$$

This formula well predicts the precision of the ML<sub>2</sub> algorithm under all the tested conditions.

### Background distribution among the ROIs of bulk-stained slices

As a next step of our analysis, we evaluate the spatial distribution of background values in different ROIs of bulk-stained tissue (Fig. 7 A) and their impact on the quantification of fluorescence measurements. We first selected ROIs at different locations of a single slice and measured the total ROI fluorescence intensities. We then estimated their in situ background values with the  $ML_2$  algorithm, the mean intensities of the 10% darkest image pixels, as well as the tissue autofluorescence taken from unstained slices (Fig. 7, B and C).

We found that under our experimental conditions, the background intensities (Fig. 7, B and C, *second column*) varied considerably among the various ROIs throughout the slice (993–2130 a.u.,  $\lambda_{ex}$ : 350 nm) and (853–1343 a.u.,  $\lambda_{ex}$ : 380 nm) (Fig. 7 C). This large variation is mostly due to an uneven distribution of extra- or intracellular dye rather than

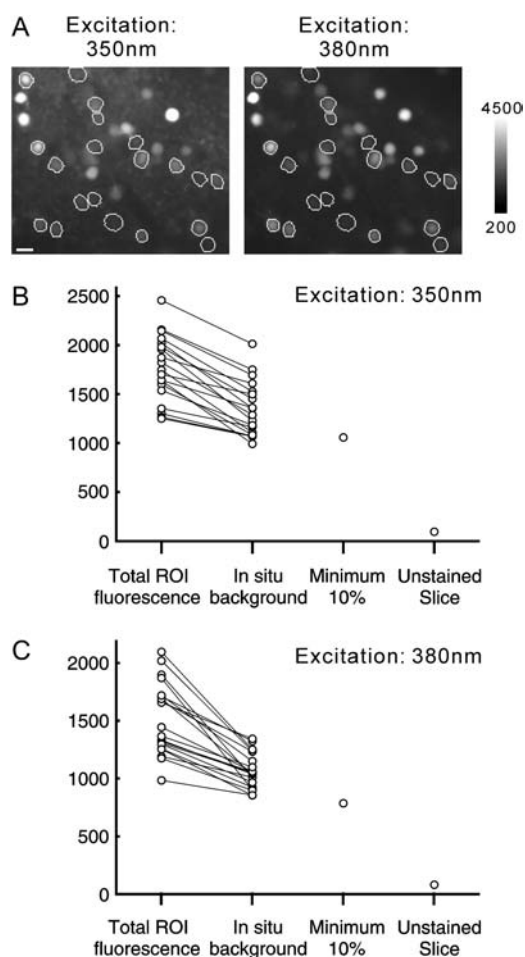


FIGURE 7 Background distribution in bulk-stained tissues. (A) FURA-2 images of an olfactory bulb slice obtained at the indicated excitation wavelengths. Scale bar, 20  $\mu\text{m}$ . (B,C) The graph shows the total fluorescence intensity of the ROIs indicated in A, their in situ background estimated using the proposed method, mean intensity of the 10% darkest image pixels, and the average autofluorescence level measured from unstained slices.

to the inhomogeneity of excitation because the maximum variation of excitation was measured to be 8.5% ( $\lambda_{ex}$ : 350 nm) or 10.2% ( $\lambda_{ex}$ : 380 nm). More importantly, the background represents a large proportion ( $70.3 \pm 15\%$ ) of the total ROI intensity (Fig. 7, B and C, *first column*), and this proportion showed a broad variation from cell to cell (27–88%). Such results underscore the importance of estimating backgrounds accurately and independently for each ROI. From this figure, it is evident that using the same background value for every cell, be it the darkest value of a slice or the average of unstained slices, leads to large errors.

### [Ca<sup>2+</sup>] quantification in bulk-stained experiments

As a typical [Ca<sup>2+</sup>] imaging experiment using FURA-2, we measured the resting [Ca<sup>2+</sup>] in olfactory bulb neurons by blocking action-potential-dependent spontaneous calcium transients with 1  $\mu\text{M}$  TTX (Fig. 8 A). [Ca<sup>2+</sup>] was quantified using the standard equation (15), with calibration constants determined in separate experiments (see Materials and Methods, above). After compensating the correct background, we found the resting [Ca<sup>2+</sup>] in the olfactory bulb neurons to be in the range of  $56 \pm 9$  nM ( $n = 9$ ; Fig. 8 B). This result is comparable with earlier estimates using single cell-staining methods in the same cell type (27), as well as in

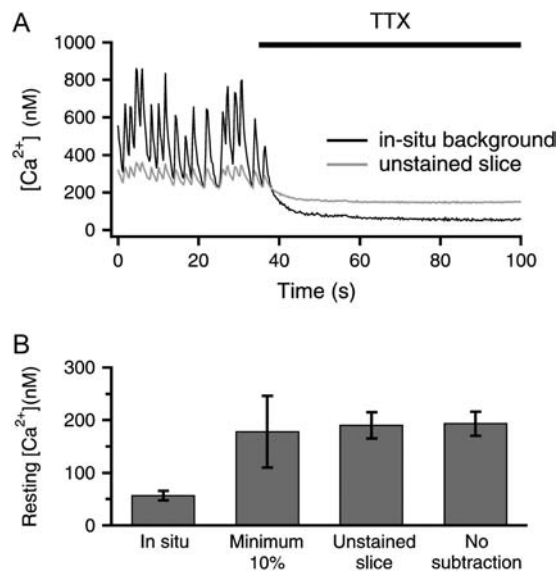


FIGURE 8 Effects of background estimation on [Ca<sup>2+</sup>] quantification. (A) TTX was used to block spontaneous-action potential-dependent [Ca<sup>2+</sup>] transients. The fluorescence ratio after subtracting the in situ background (*solid trace*) or the average fluorescence of unstained slices (*shaded trace*) were converted to [Ca<sup>2+</sup>] using the standard equation, Eq. 15. Note the uncompensated background leads to marked overestimate of [Ca<sup>2+</sup>] at low concentrations (*second half of the trace*) and an underestimate of [Ca<sup>2+</sup>] at higher [Ca<sup>2+</sup>] levels (*first half of the trace*). (B) The [Ca<sup>2+</sup>] after returning to a baseline level was taken as the resting value. It was estimated to be  $56 \pm 9$  nM ( $n = 9$ ) after subtracting the background estimated with our method. The resting [Ca<sup>2+</sup>] obtained using other background values are also shown for comparison. Error bars, mean  $\pm$  SE.

other CNS neurons (17,28). Using either a dark image region or the mean fluorescence of unstained slices as background resulted in a significant overestimate of the resting  $[Ca^{2+}]$  (Fig. 8 A, *second half*, Fig. 8 B).

Comparing the  $[Ca^{2+}]$  dynamics obtained after subtracting the correct background (Fig. 8 A, *solid curve*) or after subtracting average fluorescence of unstained slices (Fig. 8 A, *shaded curve*) showed that the  $[Ca^{2+}]$  can either be over- or underestimated depending on the concentration range. This is because incomplete background subtraction brings the fluorescence ratio closer to the ratio of the uncompensated backgrounds at the two excitation wavelengths. Therefore, at low resting  $[Ca^{2+}]$  and correspondingly small fluorescence ratios, incomplete background subtraction typically leads to an overestimation of the resting  $[Ca^{2+}]$ . However, physiological  $[Ca^{2+}]$  values often vary within a wide range, and in the middle and higher range of  $[Ca^{2+}]$ , inaccurate background subtraction frequently results in marked underestimated  $[Ca^{2+}]$  values. These deviations are clearly seen in the first half of the traces shown in Fig. 8 A. The boundary between over- and underestimation occurs where the fluorescence ratio equals the ratio of the uncompensated backgrounds, a value that differs from cell to cell. Thus, inaccurate background estimation not only introduces an error when obtaining the absolute  $[Ca^{2+}]$  values, but can also cause considerable confusion when comparing relative  $[Ca^{2+}]$  levels in different cells.

To give a specific example of such a case, we show the responses of two olfactory bulb neurons to odorant stimulation (Fig. 9 A). After the initial odorant-induced  $[Ca^{2+}]$  transient, the  $[Ca^{2+}]$  in cell 1 (Fig. 9, B and C, *solid curve*) returned to a stable value whereas cell 2 (Fig. 9, B and C, *shaded curve*) showed prolonged  $[Ca^{2+}]$  fluctuations. If the average fluorescence of unstained slices was used as background, the  $[Ca^{2+}]$  level in both cells seemed to be in a similar range (Fig. 9 B). However, a correct background subtraction clearly revealed that the  $[Ca^{2+}]$  in cell 1 returned to a near-resting level after stimulation, whereas cell 2 showed a much larger  $[Ca^{2+}]$  response and its  $[Ca^{2+}]$  remained elevated throughout the recording period (Fig. 9 C).

## DISCUSSION

Imaging techniques, such as laser scanning microscopy or CCD-based imaging, are widely used to investigate the spatiotemporal dynamics of biological systems. In many cases it can be assumed that the intensities in certain adjacent image pixels are governed by the same biophysical process. It is then permitted and advantageous to evaluate those pixels together as a region of interest. As the relevant information is distributed over all ROI pixels, it is interesting and important to ask how such information can be optimally retrieved, considering the need to minimize both unwanted background and noise.

Commonly, background and noise are dealt with separately. Averaging is first used to reduce the noise, and the background is then estimated from additional measurements and subtracted. For two reasons, this conventional approach is not optimal. First, taking separate background measurements is both time-consuming and often impractical, particularly in bulk-stained tissue; second, averaging is not the best way of noise reduction because it combines the dimmer and the brighter pixels with equal weighting factors (see next sections).

We therefore took a different approach. First, instead of viewing the imaging recordings merely as stacks of two-dimensional images, we realized the usefulness of taking into account its three-dimensional nature. Following this concept, we constructed a simple model for the intensity dynamics of individual ROI pixels and derived a statistically optimal algorithm to simultaneously minimize background and noise without using any information outside the respective ROI.

### Accuracy of the algorithm in real experiments

The performance of our background estimation algorithm in real experiments may be affected by two types of error. First, random noise leads to errors in  $\mu_i$ -estimation, which causes the estimated background to fluctuate randomly. This type of error was extensively investigated using computer simulation. Among the three algorithms compared, the  $ML_2$  algorithm is superior in that it is unbiased under all tested

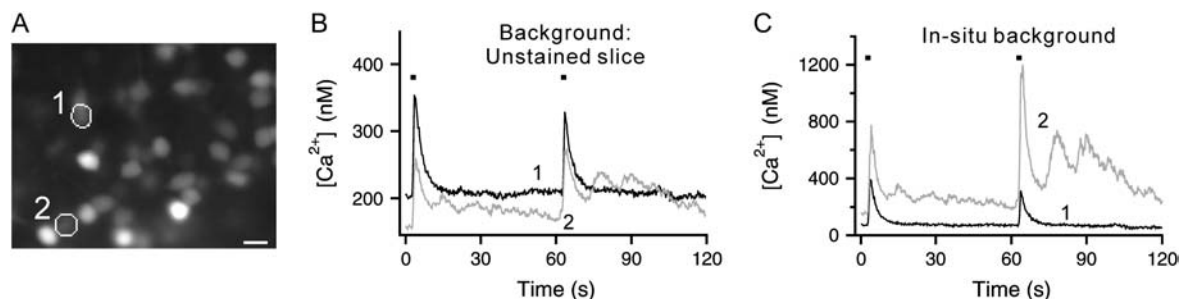


FIGURE 9 Background introduces errors in cross-cell comparison of odorant-induced  $[Ca^{2+}]$  responses. (A) Odorant stimulation induces  $[Ca^{2+}]$  response in the two olfactory bulb neurons encircled. The image shown was taken at 380-nm excitation. Scale bar, 20  $\mu\text{m}$ . (B) Odorant-stimulated  $[Ca^{2+}]$  dynamics obtained by using the fluorescence of an unstained slice as background value. (C)  $[Ca^{2+}]$  dynamics of the two cells after compensating the correct background.

conditions. The fluctuation ( $\sigma$ ) of the estimated background becomes smaller as SNR, number of timepoints ( $p$ ), number of pixels ( $q$ ), and the spread of  $u_i$  ( $CV_u$ ) increase. The dependency of  $\sigma$  on these four parameters can well be predicted by Eq. 20. For the experimental data shown in Fig. 7 ( $p = 960$ ), we calculated  $\overline{SNR}$ ,  $q$ , and  $CV_u$  for each selected ROI. The results give an averaged  $\overline{SNR}$  of 3.10 (range: 0.86–13.88), averaged  $q$  of 157 (range: 89–332), and averaged  $CV_u$  of 0.355 (range: 0.138–0.570). Using Eq. 20, the error ( $\Delta b/\bar{F}$ ) of the algorithm due to random noise was estimated to be 0.4% (range 0.04–1.17%).

The other type of error comes from intra-ROI background inhomogeneity. Our method uses a noise-dependent threshold to exclude pixels with additional background that is large enough to be distinguished from random noise. However, as noise becomes large, pixels with small additional background may fail to be detected and excluded. We estimate this type of error by performing the algorithm on randomly chosen ROI subsets that contain half the total pixel number. The standard deviation of  $\bar{f}$  obtained from different ROI subsets was used to test whether the algorithm can robustly find the same regression line. Applying this analysis to the experimental data gives an average variation of 2% (range: 0.15–5.97%). Thus, the error of the fluorescence intensity due to background inhomogeneity is <6% for all the selected ROI.

### Practical concerns

Several other factors may have an impact on the accuracy of our background estimation algorithm, which should be considered when applying the method.

First, mechanical stability of the recording should be maintained because even a slight movement of the specimen can introduce additional intensity variations other than the physiological process of interest. More importantly, in the presence of movement, the intensity traces of the ROI pixels can no longer be modeled as amplitude-scaled versions of a common function, the basic assumption of our method. Applying the algorithm to such unstable image sequences will result in an erroneous estimation of both  $u_i$  and  $\bar{f}$ , and thus a marked error in background estimation. To avoid this, care was taken in our experiments to minimize slice movements caused by either vibrations or odorant application. Recordings were discarded when a significant drift ( $>2 \mu\text{m}$ ) of the last image compared to the first image occurred. Slight movements could be corrected with image registration software; for example, Turboreg (29), an ImageJ plug-in, is very fast and gives satisfactory results.

Second, for high resolution experiments, e.g., when using a confocal microscope with high pixel resolution and a fast scanning, the pixel dwelling time may be so short that the Gaussian approximation of the photon noise is no longer valid. In such situations, it is advantageous to bin neighboring pixels together or to use a lower spatial resolution during

recording to increase the SNR in each pixel. We typically adjust our measurements such that the number of pixels per cell is in the range of 100–300 (corresponding to a spatial resolution of  $\sim 1 \mu\text{m}$ ). This resolution is more than sufficient to clearly identify individual cells and gives each pixel enough signal to apply our algorithm.

### Computational cost

Computational cost is a critical factor that determines the practical usefulness of an algorithm. In contrast to many situations where numerical optimization is required to compute the maximum likelihood estimator (30), there exists an analytical solution to our optimization problem. Moreover, highly optimized routines for the major computational steps (finding the eigenvector with maximum eigenvalue, linear fitting, etc.) can be found in most numerical libraries. Our method can thus be easily implemented and is computationally efficient. Using MatLab, we can routinely perform our algorithm in  $<1$  s for a ROI with 100–300 pixels and 480 image frames. We expect further improvement in performance by implementing the algorithm in C code. Compared to manually choosing a background region for each ROI, our method is not only unambiguous but also much faster.

### Advantage of using the ML estimator to estimate $u_i$

At the core of the proposed algorithm is an accurate and precise estimation of the signal scaling factors  $u_i$ . It is well known in signal processing theory that if the waveform to be detected is known, the amplitude of the signal can best be estimated as the inner product between the noisy data and this known waveform. This approach is known as correlation detection, or matched filter (31). A correlation detector greatly attenuates the noise by exploiting the fact that the random noise is in general uncorrelated with the signal. Thus, it allows a weak signal to be robustly detected even in a relatively noisy environment. According to this concept, if the true fluorescence signal  $\tilde{\mathbf{f}}$  is available, one can use the correlation detector to estimate  $u_i$  as  $u_{i,\text{opt}}^* = \tilde{\mathbf{y}}_i' \tilde{\mathbf{f}}$ . Such an estimator is unbiased,

$$E\{u_{i,\text{opt}}^*\} = E\{(u_i \tilde{\mathbf{f}}' + \tilde{\mathbf{n}}_i') \tilde{\mathbf{f}}\} = u_i,$$

and can be shown to have a minimal variance.

In reality, however, the true fluorescence waveform  $\tilde{\mathbf{f}}$  is not available. Nevertheless, one can recognize that the ML method first obtains a waveform  $\tilde{\mathbf{f}}_{\text{ML}}^*$  (Eq. 12) common to ROI pixels and then uses correlation detection for  $u_i$  as  $u_{i,\text{ML}}^* = \tilde{\mathbf{y}}_i' \tilde{\mathbf{f}}_{\text{ML}}^*$  (Eq. 13). This method estimates the  $u_i$  utilizing the maximum available information, and proved to give a much better result than using the standard deviation of the pixel traces  $\tilde{\mathbf{y}}_i$ . This is because, in the latter case, the standard deviation

$$(\tilde{\mathbf{y}}_i \tilde{\mathbf{y}}_i)^{\frac{1}{2}} = [(u_i \tilde{\mathbf{f}}' + \tilde{\mathbf{n}}_i')(u_i \tilde{\mathbf{f}} + \tilde{\mathbf{n}}_i)]^{\frac{1}{2}} \sim u_i \left( 1 + \frac{\tilde{\mathbf{f}}' \tilde{\mathbf{n}}_i}{u_i} + \frac{|\tilde{\mathbf{n}}_i|^2}{2u_i^2} \right) \quad (21)$$

gives

$$E\{(\tilde{\mathbf{y}}_i \tilde{\mathbf{y}}_i)^{\frac{1}{2}}\} \sim u_i + \frac{p\sigma_n^2}{2u_i} \quad (22)$$

Thus, using  $(\tilde{\mathbf{y}}_i \tilde{\mathbf{y}}_i)^{(1/2)}$  results in a noise-dependent overestimation of the true  $u_i$ , with a bias term  $(p\sigma_n^2/2u_i)$  inversely proportional to  $u_i$ . The consequence of such  $u_i$ -dependent bias is a steeper regression line and an underestimation of background (Fig. 5 A) that is unacceptable under most conditions, as is clearly shown in our simulation experiments (Fig. 6, A and B).

### Advantage of using the ML estimator to estimate $\tilde{\mathbf{f}}$

An additional advantage of using the ML method is that the estimated fluorescence waveform  $\tilde{\mathbf{f}}_{\text{ML}}^*$  shows lower noise than that obtained by averaging the ROI pixels. The latter can be viewed as a spatial low-pass filter with equal coefficients for each pixel. Consider a weighted linear combination of the fluorescence waveforms  $\tilde{\mathbf{y}}_i$  using arbitrary weighting factors  $\alpha_i$ ,

$$\tilde{\mathbf{f}}^* = \sum_{i=1}^q \alpha_i \tilde{\mathbf{y}}_i = \left( \sum_{i=1}^q \alpha_i u_i \right) \tilde{\mathbf{f}} + \sum_{i=1}^q \alpha_i \tilde{\mathbf{n}}_i.$$

The expected power of the noise term is  $E\{|\sum_{i=1}^q \alpha_i \tilde{\mathbf{n}}_i|^2\} = \sum_{i,j} \alpha_i \alpha_j E\{\tilde{\mathbf{n}}_i' \tilde{\mathbf{n}}_j\} = \sigma_n^2 (\sum_{i=1}^q \alpha_i^2)$ . Thus, the signal/noise ratio can be expressed as

$$SNR = \frac{(\sum_{i=1}^q \alpha_i u_i)^2}{\sigma_n^2 (\sum_{i=1}^q \alpha_i^2)} \leq \frac{\sum_{i=1}^q u_i^2}{\sigma_n^2} \equiv (SNR)_{\text{max}}. \quad (23)$$

The inequality follows from Cauchy-Schwartz inequality, with equality occurring as  $\alpha_i \propto u_i$ . Thus, to obtain a maximum SNR, one should choose the weights ( $\alpha_i$ ) proportional to  $u_i$  instead of using equal weights for all pixels. The result is intuitive because it tells us to trust a pixel with larger signal amplitude more than pixels with smaller amplitudes.

In reality, however, the true  $u_i$  is also not known. To understand the advantages of the ML method, one can multiply  $\tilde{\mathbf{y}}_i$  to both sides of Eq. 13 and sum over  $i$ ,

$$\sum_{i=1}^q u_{i,\text{ML}}^* \tilde{\mathbf{y}}_i = \left( \sum_{i=1}^q \tilde{\mathbf{y}}_i \tilde{\mathbf{y}}_i' \right) \tilde{\mathbf{f}}_{\text{ML}}^* = R \tilde{\mathbf{f}}_{\text{ML}}^* = \lambda_1 \tilde{\mathbf{f}}_{\text{ML}}^*. \quad (24)$$

Here,  $\lambda_1$  is the largest eigenvalue of the matrix  $R = (\sum_{i=1}^q \tilde{\mathbf{y}}_i \tilde{\mathbf{y}}_i')$ . From the above equation, we have

$$\tilde{\mathbf{f}}_{\text{ML}}^* = \frac{1}{\lambda_1} \sum_{i=1}^q u_{i,\text{ML}}^* \tilde{\mathbf{y}}_i. \quad (25)$$

Thus,  $\tilde{\mathbf{f}}_{\text{ML}}^*$  can actually be represented as a weighted linear combination of  $\tilde{\mathbf{y}}_i$  with  $u_{i,\text{ML}}^*$  as weighting factors. Such

relationship is automatically satisfied when choosing  $\tilde{\mathbf{f}}_{\text{ML}}^*$  as an eigenvector of  $R$  (Eq. 12) and  $u_{i,\text{ML}}^* = \tilde{\mathbf{y}}_i' \tilde{\mathbf{f}}_{\text{ML}}^*$  (Eq. 13). As the  $u_{i,\text{ML}}^*$  are good estimates of  $u_i$ , the SNR of  $\tilde{\mathbf{f}}_{\text{ML}}^*$  will approach the theoretical optimal value shown in Eq. 23.

To evaluate the gain in SNR using the ML method compared to averaging with equal coefficients, we note that for any particular choice of the weights  $\alpha_i$ , the deviation of the SNR from the optimal value is

$$\frac{SNR}{(SNR)_{\text{max}}} = \frac{(\sum_{i=1}^q \alpha_i u_i)^2}{(\sum_{i=1}^q \alpha_i^2) (\sum_{i=1}^q u_i^2)} = \cos^2 \theta, \quad (26)$$

where  $\theta$  is the angle between the vectors  $\{\alpha_i\}$  and  $\{u_i\}$  in  $q$ -dimensional space. Thus, the gain in SNR depends on the distribution of  $u_i$  in a particular ROI. If all the  $u_i$  are equal, averaging and the ML method gives the same SNR. On the other hand, if the  $u_i$  spread in a broad range, the SNR improvement using the ML method will be substantial. We calculated the SNR gain using the  $u_i$ -distribution from the experimental ROI data shown in Fig. 7. The results show that  $\tilde{\mathbf{f}}_{\text{ML}}^*$  gives 13.9% higher SNR in average (range: 1.9–32.5%) compared to simple averaging.

The improvements shown above are important in two respects. First, the higher SNR allows us, e.g., to reduce the CCD exposure time or excitation intensity. Second, correlation detection of  $u_i$  (Eq. 13) depends on the estimate of  $\tilde{\mathbf{f}}$ . It is therefore advantageous to use the one with the lowest possible noise.

### Applicability

In addition to calcium imaging in bulk-stained neurons, our background estimation algorithm can also be valuable in ROI-based analysis of other quantitative fluorescent measurements. In particular, recent developments in photochemistry have given birth to a variety of ratiometric fluorescent indicators for several other intracellular ions, such as  $\text{Cl}^-$  (32,33),  $\text{K}^+$  (34), and  $\text{H}^+$  (35). To fully exploit the ability of these indicators for quantitative measurements, a method to extract a background-free signal from raw-image data is essential (15). Furthermore, as in vivo multicellular dye loading (6) and genetically encoded indicators (32,35,36) continue to improve, more and more in vivo imaging experiments can be expected. The ability of our method to estimate ROI background in situ can bring substantial improvements to the quantification of those data.

Our algorithm assumes a common fluorescence waveform  $f(t)$  for pixels within a single ROI. This is an implicit assumption that has to be made in any ROI-based analysis, including averaging the ROI pixels. This assumption needs to be carefully justified. For example, when imaging the concentration of small ions, assuming one  $f(t)$  per ROI is a reasonable approximation if the ions equilibrate in the imaged compartment much faster than the camera exposure time. In our experiments, we sample the fluorescence image

at 5 Hz (100 ms exposure for each excitation wavelength). Thus, transient  $[\text{Ca}^{2+}]$  inhomogeneities near the plasma membrane (a so-called calcium microdomain) during an action potential, is unlikely to contribute significantly because it decays within a few milliseconds and is highly localized to nanometers near the calcium entry site (37). Indeed, assuming a common  $f(t)$  (Eq. 2) explained the ROI data of our experiments very well because the squared model residual (data not explained by assuming a common waveform) is only a small fraction (1.1% in average, range: 0.07–4.95%, data from Fig. 7) of the squared model signal.

Finally, note that although our method assumes the background to be stationary, this stationarity is required only for the duration of a single image sequence, not the duration of the entire experiment. For example, if the experiment consists of 20 three-minute image sessions with a total duration of 1 h, the background is assumed to be stable only within each of the three-minute periods. Thus, whenever background instabilities (e.g., due to photobleaching) are slow as compared to a single image sequence, our method can be applied and will give accurate results.

## APPENDIX A: MINIMIZATION OF EQ. 11

Here, we derive the solution of the minimization problem in Eq. 11. That is, finding the scaling factors  $u_i$  for each of the  $q$  ROI pixels and  $\tilde{\mathbf{f}} \in W^\perp$ , such that  $S = \sum_{i=1}^q |\tilde{\mathbf{y}}_i - u_i \tilde{\mathbf{f}}|^2$  is minimized under the constraint  $|\tilde{\mathbf{f}}|^2 = 1$ .

For any given unit vector  $\tilde{\mathbf{f}}$ , the distance  $|\tilde{\mathbf{y}}_i - u_i \tilde{\mathbf{f}}|$  between the vectors  $\tilde{\mathbf{y}}_i$  and  $u_i \tilde{\mathbf{f}}$  is minimized if  $u_i \tilde{\mathbf{f}}$  equals the orthogonal projection of  $\tilde{\mathbf{y}}_i$  along the direction of  $\tilde{\mathbf{f}}$ , i.e., if  $u_i = \tilde{\mathbf{f}}' \tilde{\mathbf{y}}_i$ . Thus,  $|\tilde{\mathbf{y}}_i - u_i \tilde{\mathbf{f}}|^2 \geq |\tilde{\mathbf{y}}_i - \tilde{\mathbf{f}} \tilde{\mathbf{f}}' \tilde{\mathbf{y}}_i|^2$ . Therefore we have

$$\begin{aligned} S &= \sum_{i=1}^q |\tilde{\mathbf{y}}_i - u_i \tilde{\mathbf{f}}|^2 \geq \sum_{i=1}^q |\tilde{\mathbf{y}}_i - \tilde{\mathbf{f}} \tilde{\mathbf{f}}' \tilde{\mathbf{y}}_i|^2 \\ &= \sum_{i=1}^q |\tilde{\mathbf{y}}_i|^2 - \tilde{\mathbf{f}}' \left( \sum_{i=1}^q \tilde{\mathbf{y}}_i \tilde{\mathbf{y}}_i' \right) \tilde{\mathbf{f}} \\ &= \sum_{i=1}^q |\tilde{\mathbf{y}}_i|^2 - \tilde{\mathbf{f}}' \mathbf{R} \tilde{\mathbf{f}}. \end{aligned} \quad (27)$$

The first term is constant. For  $S$  to be minimized, we have to maximize  $\tilde{\mathbf{f}}' \mathbf{R} \tilde{\mathbf{f}}$  over all vectors  $\tilde{\mathbf{f}} \in W^\perp$  of unit length.

As  $\mathbf{R}$  is a symmetric matrix, it has real eigenvalues. Let  $\mathbf{R} = \mathbf{B} \mathbf{A} \mathbf{B}'$  be the eigenvalue decomposition of  $\mathbf{R}$  where  $\mathbf{B} = [\beta_1, \beta_2, \dots, \beta_p]$  are eigenvectors and  $\mathbf{A} = \text{diag}(\lambda_1, \lambda_2, \dots, \lambda_p)$  is a diagonal matrix with corresponding eigenvalues in descending order. Let  $\mathbf{g} = \mathbf{B}' \tilde{\mathbf{f}}$ , we have

$$\tilde{\mathbf{f}}' \mathbf{R} \tilde{\mathbf{f}} = \mathbf{g}' \mathbf{A} \mathbf{g} = \sum_i \lambda_i g_i^2 \leq \lambda_1 \mathbf{g}' \mathbf{g} = \lambda_1, \quad (28)$$

with equality when  $g_1 = 1$ , and  $g_2 = g_3 = \dots = g_p = 0$ , that is, when  $\tilde{\mathbf{f}} = \beta_1$ . Finally, if  $\lambda_1 \neq 0$ , it can be shown that  $\beta_1 \in W^\perp$  because it is an eigenvector of the matrix  $\mathbf{R} = (\sum_{i=1}^q \tilde{\mathbf{y}}_i \tilde{\mathbf{y}}_i')$  where  $\tilde{\mathbf{y}}_i \in W^\perp \forall i$ . Thus,  $\tilde{\mathbf{f}}^* = \beta_1$  and  $u_i^* = \tilde{\mathbf{y}}_i' \tilde{\mathbf{f}}^*$  is the solution of the minimization problem and the desired ML estimator for the parameters  $u_i$  and  $\tilde{\mathbf{f}}$ .

## APPENDIX B: VARIATION OF $D_i$ UNDER HOMOGENEOUS BACKGROUND ASSUMPTION

Even when the background is homogeneous within a ROI, the  $(\bar{y}_i, u_i^*)$  pairs do not perfectly fall on a straight line because both  $\bar{y}_i$  and  $u_i^*$  are derived

from data and thus contain noise. In other words, the vertical distances of the data pairs from the regression line,  $d_i = \bar{y}_i - u_i^* \bar{f} - b$ , fluctuates around zero. To determine whether the observed  $d_i$  can be explained by random noise alone or whether an additional background has to be assumed, the variation of  $d_i$  under homogeneous background assumption needs to be estimated. Using Eq. 3 for  $\bar{y}_i$ , we have

$$d_i = (u_i - u_i^*) \bar{f} - \bar{n}_i = (u_i - u_i^*) \bar{f} - \frac{1}{p} \mathbf{1}'_p \mathbf{n}_i. \quad (29)$$

Inserting Eq. 4 into Eq. 13, we have

$$\begin{aligned} u_i^* &= (u_i \tilde{\mathbf{f}}' + \tilde{\mathbf{n}}_i') \tilde{\mathbf{f}}^* \\ &= (u_i \tilde{\mathbf{f}}' + \tilde{\mathbf{n}}_i') (\tilde{\mathbf{f}} + \delta \tilde{\mathbf{f}}) \\ &= u_i + u_i \tilde{\mathbf{f}}' \delta \tilde{\mathbf{f}} + \tilde{\mathbf{n}}_i' \tilde{\mathbf{f}} + \tilde{\mathbf{n}}_i' \delta \tilde{\mathbf{f}} \\ &\sim u_i + \tilde{\mathbf{n}}_i' \tilde{\mathbf{f}}. \end{aligned} \quad (30)$$

Here,  $\delta \tilde{\mathbf{f}} \equiv (\tilde{\mathbf{f}}^* - \tilde{\mathbf{f}})$  is the deviation of  $\tilde{\mathbf{f}}^*$  from the true  $\tilde{\mathbf{f}}$ . Since  $|\tilde{\mathbf{f}}^*|^2 = |\tilde{\mathbf{f}} + \delta \tilde{\mathbf{f}}|^2 = 1$ , we have  $\tilde{\mathbf{f}}' \delta \tilde{\mathbf{f}} \sim 0$  when ignoring the  $|\delta \tilde{\mathbf{f}}|^2$  term. We also left out the second-order noise term  $\tilde{\mathbf{n}}_i' \delta \tilde{\mathbf{f}}$ . Combining Eqs. 29 and 30, we have

$$\begin{aligned} d_i &\sim -(\tilde{\mathbf{n}}_i' \tilde{\mathbf{f}}) \bar{f} - \frac{1}{p} \mathbf{1}'_p \mathbf{n}_i, \\ &= -[\mathbf{n}_i - \left(\frac{1}{p} \mathbf{1}'_p \mathbf{n}_i\right) \mathbf{1}_p]' \tilde{\mathbf{f}} \bar{f} - \frac{1}{p} \mathbf{1}'_p \mathbf{n}_i, \\ &= -(\tilde{\mathbf{f}} \tilde{\mathbf{f}} + \frac{1}{p} \mathbf{1}'_p) n_i, \end{aligned}$$

thus

$$E\{d_i^2\} \sim (\tilde{\mathbf{f}} \tilde{\mathbf{f}} + \frac{1}{p} \mathbf{1}'_p)' E\{\mathbf{n}_i \mathbf{n}_i'\} (\tilde{\mathbf{f}} \tilde{\mathbf{f}} + \frac{1}{p} \mathbf{1}'_p) = (\bar{f}^2 + \frac{1}{p}) \sigma_n^2.$$

We thank S. Junek for helpful comments and discussions, and H. Schultens for reading the manuscript.

This work was supported by the Deutschen Forschungsgemeinschaft Center for Molecular Physiology of the Brain (I.4) and the Bernstein Center for Computational Neuroscience (grant No. 01GQ0432).

## REFERENCES

1. Kenet, T., D. Bibitchkov, M. Tsodyks, A. Grinvald, and A. Arieli. 2003. Spontaneously emerging cortical representations of visual attributes. *Nature*. 425:954–956.
2. Ikegaya, Y., G. Aaron, R. Cossart, D. Aronov, I. Lampl, D. Ferster, and R. Yuste. 2004. Synfire chains and cortical songs: temporal modules of cortical activity. *Science*. 304:559–564.
3. Ohki, K., S. Chung, Y. Ch'ng, P. Kara, and R. Reid. 2005. Functional imaging with cellular resolution reveals precise micro-architecture in visual cortex. *Nature*. 433:597–603.
4. Tsien, R. 1981. A nondisruptive technique for loading calcium buffers and indicators into cells. *Nature*. 290:527–528.
5. Haugland, R. P. 2002. Handbook of Biological Fluorescent Probes and Research Products. Molecular Probes, Eugene, OR.
6. Stosiek, C., O. Garaschuk, K. Holthoff, and A. Konnerth. 2003. In vivo two-photon calcium imaging of neuronal networks. *Proc. Natl. Acad. Sci. USA*. 100:7319–7324.
7. Mao, B. Q., F. Hamzei-Sichani, D. Aronov, R. C. Froemke, and R. Yuste. 2001. Dynamics of spontaneous activity in neocortical slices. *Neuron*. 32:883–898.

8. Garaschuk, O., J. Linn, J. Eilers, and A. Konnerth. 2000. Large-scale oscillatory calcium waves in the immature cortex. *Nat. Neurosci.* 3:452–459.
9. Niell, C., and S. Smith. 2005. Functional imaging reveals rapid development of visual response properties in the zebrafish tectum. *Neuron.* 45:941–951.
10. Kirischuk, S., and A. Verkhratsky. 1996.  $[Ca^{2+}]_i$  recordings from neural cells in acutely isolated cerebellar slices employing differential loading of the membrane permeant form of the calcium indicator FURA-2. *Pflugers Arch. Eur. J. Physiol.* 431:977–983.
11. Brooke, S. M., J. A. Trafton, and R. M. Sapolsky. 1996. Auto-fluorescence as a confound in the determination of calcium levels in hippocampal slices using FURA-2/AM dye. *Brain Res.* 706:283–288.
12. Yasuda, R., E. Nimchinsky, V. Scheuss, T. Pologruto, T. Oertner, B. Sabatini, and K. Svoboda. 2004. Imaging calcium concentration dynamics in small neuronal compartments. *Sci. STKE.* 219:15.
13. Virgilio, F. D., T. Steinberg, and S. Silverstein. 1990. Inhibition of FURA-2 sequestration and secretion with organic anion transport blockers. *Cell Calcium.* 11:57–62.
14. Kao, J. 1994. Practical aspects of measuring  $[Ca^{2+}]_i$  with fluorescent indicators. *Methods Cell Biol.* 40:155–181.
15. Grynkiewicz, G., M. Poenie, and R. Y. Tsien. 1985. A new generation of  $Ca^{2+}$  indicators with greatly improved fluorescence properties. *J. Biol. Chem.* 260:3440–3450.
16. Minta, A., J. Kao, and R. Tsien. 1989. Fluorescent indicators for cytosolic calcium based on rhodamine and fluorescein chromophores. *J. Biol. Chem.* 264:8171–8178.
17. Maravall, M., Z. F. Mainen, B. L. Sabatini, and K. Svoboda. 2000. Estimating intracellular calcium concentrations and buffering without wavelength ratioing. *Biophys. J.* 78:2655–2667.
18. Tamhane, A. C., and D. D. Dunlop. 2000. *Statistics and Data Analysis.* Prentice Hall, Englewood Cliffs, NJ.
19. van de Beek, J., M. Sandell, and P. Borjesson. 1997. ML estimation of time and frequency offset in OFDM systems. *IEEE Trans. Signal Process.* 45:1800–1805.
20. Sankar, A., and C. Lee. 1996. A maximum-likelihood approach to stochastic matching for robust speech recognition. *IEEE Trans. Speech Audio Process.* 4:190–202.
21. Ideker, T., V. Thorsson, A. Siegel, and L. Hood. 2000. Testing for differentially expressed genes by maximum-likelihood analysis of microarray data. *J. Comput. Biol.* 7:805–817.
22. Kemere, C., K. Shenoy, and T. Meng. 2004. Model-based neural decoding of reaching movements: a maximum likelihood approach. *IEEE Trans. Biomed. Eng.* 51:925–932.
23. Nieuwkoop, P. D., and J. Faber. 1956. *Normal Table of Xenopus laevis (Daudin).* North-Holland, Amsterdam, The Netherlands.
24. Czesnik, D., W. Rossler, F. Kirchner, A. Gennerich, and D. Schild. 2003. Neuronal representation of odourants in the olfactory bulb of *Xenopus laevis* tadpoles. *Eur. J. Neurosci.* 17:113–118.
25. Schild, D., A. Gennerich, and H. A. Schultens. 1996. Microcontrollers as inexpensive pulse generators and parallel processors in electrophysiological experiments. *Med. Biol. Eng. Comput.* 34:305–307.
26. Manzini, I., W. Rossler, and D. Schild. 2002. cAMP-independent responses of olfactory neurons in *Xenopus laevis* tadpoles and their projection onto olfactory bulb neurons. *J. Physiol. Lond.* 545:475–484.
27. Bischofberger, J., and D. Schild. 1995. Different spatial patterns of  $[Ca^{2+}]_i$  increase caused by N- and L-type  $Ca^{2+}$  channel activation in frog olfactory bulb neurones. *J. Physiol. (Lond.)* 487:305–317.
28. Helmchen, F., K. Imoto, and B. Sakmann. 1996.  $Ca^{2+}$  buffering and action potential-evoked  $Ca^{2+}$  signaling in dendrites of pyramidal neurons. *Biophys. J.* 70:1069–1081.
29. Thévenaz, P., U. Ruttimann, and M. Unser. 1998. A pyramid approach to subpixel registration based on intensity. *IEEE Trans. Image Process.* 7:27–41.
30. Mendel, J. M. 1995. *Lessons in Estimation Theory for Signal Processing, Communications, and Control.* Prentice Hall, Englewood Cliffs, NJ.
31. Haykin, S. 1994. *Communication Systems,* 3rd Ed. John Wiley & Sons, New York.
32. Kuner, T., and G. Augustine. 2000. A genetically encoded ratiometric indicator for chloride: capturing chloride transients in cultured hippocampal neurons. *Neuron.* 27:447–459.
33. Jayaraman, S., P. Haggie, R. Wachter, S. Remington, and A. Verkman. 2000. Mechanism and cellular applications of a green fluorescent protein-based halide sensor. *J. Biol. Chem.* 275:6047–6050.
34. Baruah, M., W. Qin, R. Vallee, D. Beljonne, T. Rohand, W. Dehaen, and N. Boens. 2005. A highly potassium-selective ratiometric fluorescent indicator based on BODIPY azacrown ether excitable with visible light. *Org. Lett.* 7:4377–4380.
35. Hanson, G., T. McAnaney, E. Park, M. Rendell, D. Yarbrough, L. X. S. Chu, S. Boxer, M. Montrose, and S. Remington. 2002. Green fluorescent protein variants as ratiometric dual emission pH sensors. 1. Structural characterization and preliminary application. *Biochemistry.* 41:15477–15488.
36. Demaurex, N. 2005. Calcium measurements in organelles with  $Ca^{2+}$ -sensitive fluorescent proteins. *Cell Calcium.* 38:213–222.
37. Shuai, J., and I. Parker. 2005. Optical single-channel recording by imaging  $Ca^{2+}$  flux through individual ion channels: theoretical considerations and limits to resolution. *Cell Calcium.* 37:283–299.